# Design and Simulation of Sun Position Sensors for Space Applications: A Comparative Study

Martha Díaz Salazar[a,b], Nadia Kondratiuk[a,b], Analía Moreno[a,b], Mónica Martínez Bogado[a,b], Sonnia Pavoni Oliver[c], Mariana Tamasi[a,b]

[a] Departamento Energía Solar- Comisión Nacional de Energía Atómica (CNEA), General Paz 1499 CP1650, San Martín, Buenos Aires, Argentina. Tel. +5467727199

[b] Instituto Nanociencia y Nanotecnología (INN)- Consejo Nacional de Investigaciones Científicas y Técnicas (CONICET), General Paz 1499 CP1650, San Martín, Buenos Aires, Argentina

[c] Centro de Investigaciones en Microelectrónica (CIME) – Universidad Tecnológica de la Habana José A. Echeverría (CUJAE), La Habana, Cuba

e-mail: marthadiazsalazar@cnea.gob.ar

## ABSTRACT

Sun position sensors are used in space applications as part of the attitude determination and control system (ADCS). The aim of this work is to describe the design process of single and dual axis sun position sensors based on a photodiode array detector and a window to limit and direct the light that reaches the detector. The design process involves choosing the sensor architecture, modeling its output, and then evaluating the model through simulation. Six architectures, with different configurations and geometries for both detector and window, were modeled and compared. To evaluate the model and performance of the sensor a program was developed, and simulations were made varying window height and size, as well as the photodiodes size. From the simulations performed we concluded that for each design, the key factors that influence the sensitivity and field of view performance are the windows height, and window or photodiode size, depending on the sensor configuration. From the comparison across architectures, the detector configuration, as well as the windows geometry, influence the sensitivity and linearity of the response for similar conditions of operation. The two-quadrant detector configuration offers a better sensitivity than the triangular photodiode configuration. For a better linearity of the output a square window is preferred. This comparative study is part of the development of new products for space applications in the National Atomic Energy Commission (CNEA) and contributes to the Argentinian National Space Plan.

Keywords: sun sensor, position sensor, design, simulation, silicon sensor.

## I. INTRODUCTION

Sun position sensors are used to measure the position of the Sun in a given frame of reference. These sensors are used in space applications as part of the attitude determination and control system (ADCS), for orientation of solar panels, or for the protection of instruments sensitive to solar radiation, among other applications.

In the literature, there are different technological alternatives regarding the structure and the structure and configuration of these sensors. Some studies propose the use of commercially available components to detect light, such as CCD (Wei et al., 2011), (Celebi & Gulmammadov, 2016) (Antonello et al., 2018), CMOS image sensors (Kim, 2021) or active pixel sensors (APS) (Buonocore et al., 2005), position sensitive detectors (PSD) (Pereira et al., 2017), linear photodiodes arrays (Diriker, 2021) or independent photodiodes. In other cases, the detector is specifically manufactured for this purpose, like in (Romijn et al., 2023) where a silicon carbide detector is elaborated to measure the position of the Sun from UV measurements. Sun position sensor based on UV detector were also found for terrestrial applications in (Jamroen et al., 2021). It is also found sun sensors with optical components developed for specific missions, like in (Boslooper et al., 2012) for a Mercury mission. For more examples, (Salgado-Conrado, 2018) presents a summary of the state of the art of sun position sensors for terrestrial and space applications, where different technologies, materials, and operating principles are described. Sun sensors are widely used in spacecrafts, Yost et al., 2021, presents the state of the art of commercial sun sensors for small spacecraft; the commercial sun sensor with a four-quadrant detector that exhibits the best trade-off between field of view (FOV) and accuracy has 0.2° accuracy within a 64° FOV. The design of the instrument determines its features, such as whether the measurement can be performed on one or two axes, the sensor's field of view, sensitivity, and linearity of the response.

In Argentina, the Solar Energy Department (*Departamento Energía Solar*, DES) of the National Atomic Energy Commission (*Comisión Nacional de Energía Atómica*, CNEA) has a vast experience in the development of photovoltaic sensors to measure global radiation and photosynthetically active radiation (PAR) at the terrestrial level, as well as in the development of coarse sun sensors (CSS) for space application (Bolzi et al., 2013 and Bogado et al., 2015).

These sensors have a space heritage of more than 20 years and 1 800 000 flight hours until July 2023. They have been part of Aquarius/SAC-D, SAOCOM 1A and 1B satellites among others (Alurralde et al., 2013) and (Bolzi et al., 2002). It is worth noting that the DES is the only research group that develops solar radiation measurement instruments and sun sensors in Argentina.

The specific challenge addressed by the study is to manufacture a sun position sensor with better accuracy than the CSS manufactured in CNEA that can achieve a three-dimensional representation of the Sun's position. One of the reasons for desiring a wide FOV is that less sensors will be required to cover the full screen, reducing the costs of the satellite (Leijtens et al., 2021).

The designs of sun position sensors proposed in this work are based on the experience acquired in the design and manufacture of photovoltaic radiometers and CSS, more precisely in the experience gained in the development of crystalline silicon photodiodes for space applications and the customization of the product to meet the needs of the mission.

This development contributes to the national space plan as we increase the offer of products we can supply to the national space industry. It also contributes to other lines of work of CNEA such as terrestrial solar trackers for measurement and characterization of solar radiation (Gröbner et al., 2019) (Bastida et al., 2022) in our country.

This paper describes the design process of sun sensors to measure the Sun's position, for which different configurations of single and dual axis sensor are proposed with the aim of obtaining the design that offers the best performance and that is suitable for the existing manufacturing technological capabilities in CNEA.

## II. SENSORS GENERAL DESIGN

To measure the position of the Sun with a better accuracy than the CSS previously elaborated in CNEA, we propose that the principle of operation of the sensor is modified from a cosine detector to a comparison between the illuminated area on different the photodiodes. The premise we adopt with this approach is that greater sensitivity in the sensor response translates to higher accuracy in measuring the position of the Sun. For this purpose, the detector is modified to have more photodiodes, and an optical component is added to the sensor to define the illuminated area. As the design must agree with the technological capabilities of CNEA we also consider how to make a detector where the separation between photodiodes isn't a constraint of the sensor response.

The proposed design consists of a detector sensitive to solar radiation and an optical component that limits and directs the light that reaches the detector. To limit and direct the light, it is used a window separated from the detector. The window proposed is an aperture in a thin metal layer evaporated on a glass substrate. The thickness of this layer is designed to be approximately 500 nm. The metal used for the window must have good adherence with the glass such as Cr. The separation between the window and the detector is defined by the thickness of the glass substrate.

The detector is formed by an array of photodiodes. For the sake of detector flatness, the array of photodiodes is designed to be integrated into a crystalline silicon (Si-c p-type) substrate. The photodiodes are formed by an $n^+pp^+$ junction that is elaborated by employing local dopant diffusion, for this purpose a $SiO_2$ barrier is used. The $SiO_2$ barrier is defined through a photolithography process and a chemical etching. The photodiode contacts are formed by a metallic multilayer of Ti/Pd/Ag. A cross-section of an array of two photodiodes is presented in Fig. 1. The detector total area is limited to a square of 12 x 12 $mm^2$, taking as reference the size of the CSS developed in the DES (Bolzi et al., 2013).

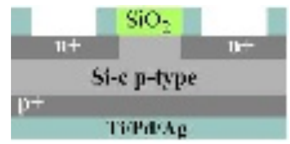

Fig. 1: Cross-section of a detector, array of two photodiodes.

The measurement principle of a photodiode states that its short circuit current ($I_{SC}$) is proportional to the illuminated area, its short-circuit current density ($J_{SC}$), and the cosine of the incidence angle ($\vartheta_i$) of the radiation, Eq. (1). The $\cos(\vartheta_i)$ factor expresses that the illuminated area is not the relevant property, but its projection in the plane normal to the direction of the incident radiation, this is known as Lambert's cosine law (Smets et al., 2016).

$$I_{SC} = J_{SC} * A_{illuminated} * \cos(\vartheta_i) \qquad (1)$$

The proposed sensors measure the position of the Sun based on the comparison of the illuminated area on each photodiode of the detector, which is mainly defined by the geometry of the window and the photodiodes. To measure the position of the Sun based on the incidence angle of the solar radiation, it is necessary to parameterize its position. A celestial sphere of arbitrary radius with the sensor at its center (Fig. 2) is used to describe the position of the star in the sensor reference frame, where the fundamental plane is the sensor plane. The position of the Sun can be parameterized based on the azimuth and zenith angles.

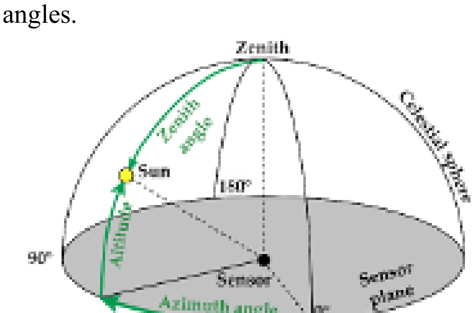

Fig. 2: Sun position representation in the sensor reference frame.

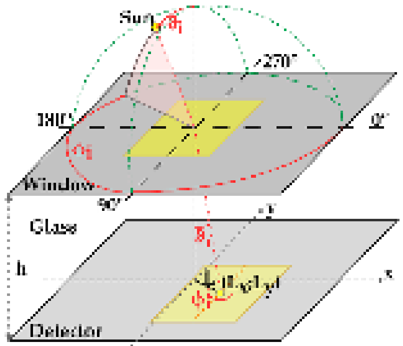


Fig. 3: General configuration of a sun sensor and parameterization of the position of the Sun in the sensor reference frame.

The altitude is the angular elevation of the center of the solar disk above the sensor plane, while the azimuthal angle ($\phi$) corresponds to the angle of the line of sight projected on the sensor plane measured clockwise. The zenith angle corresponds to the angle between the Sun and the normal of the sensor plane, it corresponds to the incidence angle ($\vartheta_i$) that was defined in Eq. (1). In this representation, the position of the Sun is defined between 0 and 90° of the zenith angle and between 0 and 360° of the azimuth angle.

The general proposed design is shown in Fig. 3, the sensors are made up of a window that limits and directs the light, a glass of thickness $h$, and the detector. To analyze the illuminated area on the detector's photodiodes, the position of the center of the light beam ***L* (*L*$_X$, *L*$_Y$)** is defined in the detector plane with respect to the position of the beam in normal incidence ($\vartheta_i = 0°$), as shown in Fig. 3. To parameterize the position of the center of the light beam that reaches the detector, it must be considered the Snell's Law, Eq. (2) because the light passes through different mediums. In Eq. (2), $n_1$ and $n_2$ are the refractive indices of air and glass respectively and $\vartheta_r$ is the angle of refraction of light in the glass.

$$n_1 * sin(\vartheta_i) = n_2 * sin(\vartheta_r) \tag{2}$$

The distance from the center of the beam to the center of the detector plane, $L$, is defined in Eq. (3), disregarding the gap between the glass and the detector. The coordinates $L_X$ and $L_Y$ are related to the refracted zenith angle ($\vartheta_r$) and the azimuthal angle ($\phi$) according to Eqs. (4) and (5). In Fig. 3 representation, when $\varphi$ is 0° and $\theta$ is increased, $L_X$ will have a negative value.

$$L = h * \tan\vartheta_r \tag{3}$$
$$L_x = -L * \cos\varphi \tag{4}$$
$$L_y = L * \sin\varphi \tag{5}$$

The field of view (FOV) of the sensor is defined as the maximum zenith angle detected by the sensor, Eq. (6). The FOV can be obtained from the maximum value of $L$, which depends on the sensor configuration or architecture, and it is analyzed for each design. From Eqs. (3) and (6), it can be concluded that the FOV of the sensor is inversely proportional to the height of the glass. Although the design of the sensor housing is not part of this work, its layout must be considered when determining the effective FOV of the sensor.

$$FOV = \vartheta_i^{MAX} \tag{6}$$

The sensor sensitivity quantifies how changes in the input signal impact the sensor's output. In the case of a linear output, sensitivity corresponds to the slope of the output response. Referring to Eq. 3, we anticipate that using thicker glass will result in larger variations in the position of the beam's center for variations in $\vartheta$. Consequently, this leads to improved sensitivity in the sensor's output.

In the following sections, the design, modeling, and simulation evaluation of different proposals for a sun position sensor with the structure of Fig. 3 are presented. Different configurations and geometries were defined for both the detector and the window, and possible variants were analyzed based on the quantity and separation of the photodiodes in the detector.

To simulate the response of the different sensor architectures a program, based on the proposed models for each design, was developed in Python. The flowchart of the program is presented in Fig. 4.

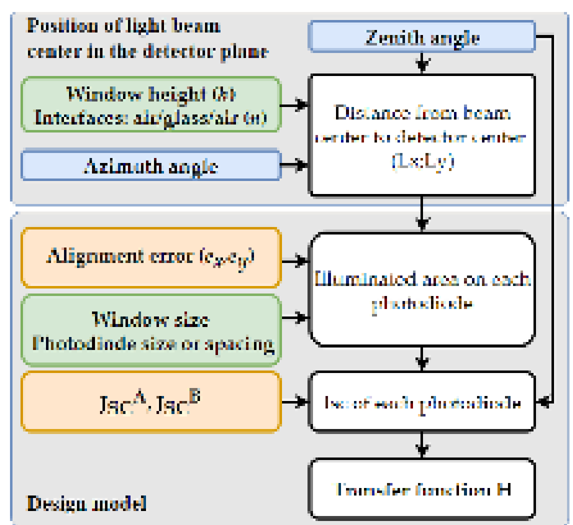


Fig. 4: Flowchart of the program developed to simulate the different designs.

The first part of the program models the input parameter, the zenith and azimuth angles of the Sun, and transforms them into the position of the center of the light beam in the detector plane. The second part of the program calculates the illuminated area on each photodiode of the detector based on the specific model of each configuration. To enhance the simulation results some inputs were added to the model, such as the possible differences in the $J_{SC}$ of the photodiodes and possible misalignments between the windows and the detector. The input variables that define the position of the Sun are highlighted in blue, the parameters defined in the design are highlighted in green, and in orange the manufacturing parameter that influences the current of each photodiode.

To evaluate the models and performance of the sensor configurations, simulations are made varying the windows height and size, as well as the detector's photodiodes size. For the $I_{SC}$ simulation, the electrical behavior under space conditions (AM0 and irradiance of 1367 W/m$^2$) of the CSS elaborated in the DES was taken as a reference due to the large number of measurements available, and a $J_{SC}$ of approximately 35 mA/cm$^2$ was considered.

The criteria for evaluating the performance of each design are to analyze its FOV, linearity, and sensitivity, for which we use linear regression of the transfer function. From the simulations of the different configurations, their advantages and disadvantages were analyzed.

The specific manufacturing parameters such as separation between photodiodes, contacts width, and total area of the detector of the sensors were determined based on the experience of manufacturing CSS and the available technology at CNEA, in the Photovoltaic Laboratory of the DES and the Clean Room of the Department of Micro and Nanotechnology (*Departamento de Micro y Nanotecnologías*, DMN) of CNEA. Other manufacturing parameters such as active area of the photodiodes, windows size, and glass thickness are defined based on the simulation results.

## III. SINGLE-AXIS SUN POSITION SENSOR

In the single-axis sun position sensor, the illuminated area on each photodiode will depend only on the variations of the light beam center position on one axis of the detector plane. With this principle, it is not possible to determine the zenith and azimuth angles of the Sun with a single sensor. To have a complete representation of the Sun's position, it is necessary to use two single-axis sensors, with their measurement axes oriented perpendicularly.

For the measurement of the Sun's position in a single-axis, two proposals were designed. In both cases, the detector is an array of two photodiodes integrated on a silicon substrate. The sensor output is obtained by comparing the illuminated area on each photodiode. The main difference between them lies in how the illuminated area on each photodiode varies as a function of the incident angle of the radiation. The first proposal uses a two-quadrant detector, and the second one uses a triangular photodiode.

### A. Design of the single-axis sun position sensor with a two-quadrant detector

In the first proposed single-axis sun sensor design, the detector is formed by two semicircular photodiodes forming two quadrants. For this design we must consider that the active area of each photodiode exceeds the area of the window. The illuminated area on each photodiode is defined by the geometry of the window (Fig. 5) and it is independent from the photodiode size. The separation between photodiodes is aligned with the y-axis of the detector plane, so that the sensor only detects variations in the x-component of the position of the light beam center, $L_X$, Eq. (4).

The analysis of the sensor response is presented when using a window with square or circular geometry, as shown in Fig. 5(c) and 5(d) respectively, where $L_X$ has a positive value. In addition, an analysis of how the sensor response varies by modifying the height of the window is presented.

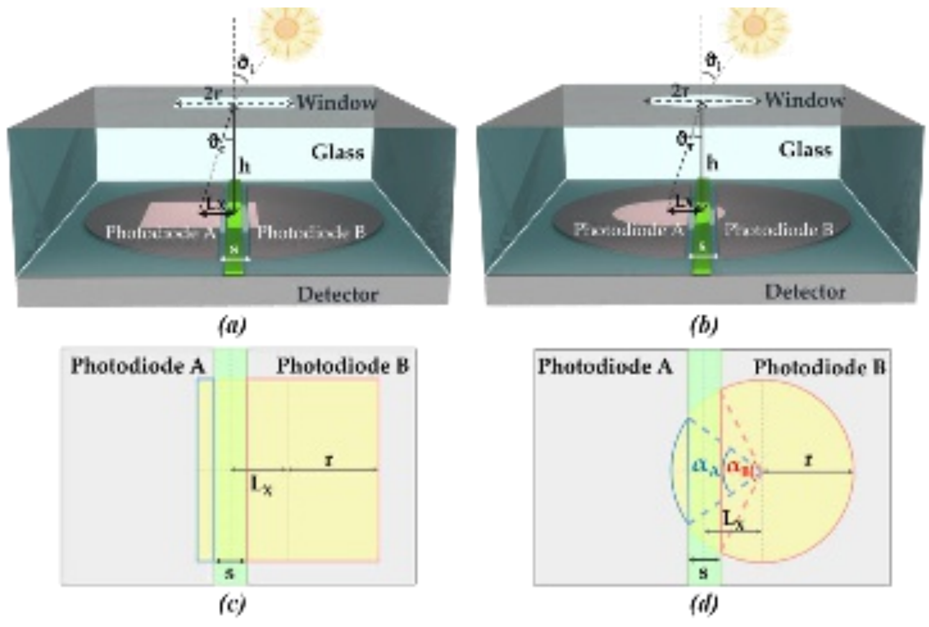


Fig. 5: Perspective and top views of the single-axis sun sensor design with a two-quadrant detector, with a square window, (a) and (c), and a circular window, (b) and (d).

As observed in the design of the sensor presented in Fig. 5, the active areas of the photodiodes are separated by a distance ***s***, defined by the width of the contacts and the silicon dioxide ($SiO_2$) barrier that is used to locally elaborate the photodiodes. The cross-section of both window geometries has a width $2r$ and the center of the window is aligned with the midpoint between the photodiodes. When $\vartheta_i$ is 0°, the illuminated area is equal in both photodiodes, and when $\vartheta_i$ increases at $\varphi$=0°, $L_X$ varies and the illuminated area on photodiode A increases while it decreases on photodiode B.

The limit in the detection of the Sun's position with this architecture is given by the angle at which one of the photodiodes is not illuminated, which corresponds to $L_X^{MAX}$, and it is defined by Eq. (7). It is important to note that in this design the FOV may be limited by the separation between photodiodes, for it is desirable to minimize this separation. In this detector configuration, the photodiode size and geometry must be chosen to ensure that at $L_X^{MAX}$ the light beam doesn't reach the border of the photodiode.

$$L_X^{max}{}_{2C} = r - \frac{s}{2} \tag{7}$$

If a square window of side *2r* is used, Fig. 5(c), the illuminated area on each photodiode as a function of the incident angle of radiation, is a rectangle of area defined in Eqs. (8) and (9) for each photodiode.

$$A_B = 2r * \left(r + L_x - \frac{s}{2}\right) \tag{8}$$

$$A_A = 4r^2 - 2r * \left(r + L_x + \frac{s}{2}\right) \tag{9}$$

With a circular window, the illuminated area on each photodiode is the portion of the circle between the chord defined by the edge of the photodiode and the corresponding arc. The illuminated area in photodiode A can be modeled as the area of the circular segment defined by the central angle $\alpha_A$, as expressed in Eq. (10), while in photodiode B, it can be described as the total window area minus the circular segment defined by $\alpha_B$, as shown in Eq. (11). The central angles $\alpha_A$ and $\alpha_B$ are obtained from Eqs. (12) and (13), considering the distance from the circle center to the chord.

$$A_{seg}^{A} = \frac{1}{2} * r^2 * (\alpha_A - \sin\alpha_A) \tag{10}$$

$$A_{seg}^{B} = \pi * r^2 - \frac{1}{2} * r^2 * (\alpha_B - \sin\alpha_B) \tag{11}$$

$$\alpha_A = 2 * \arccos\left(\frac{L_x + \frac{s}{2}}{r}\right) \tag{12}$$

$$\alpha_B = 2 * \arccos\left(\frac{L_x - \frac{s}{2}}{r}\right) \tag{13}$$

The sensor response is obtained by comparing the illuminated area on each photodiode. With this objective, it is proposed to analyze the difference between the short-circuit current ($I_{SC}$) of each photodiode, which according to Eq. (1) does not only depend on the illuminated area. To obtain a transfer function of the sensor with a two-quadrant detector ($H_{2C}$) that only depends on the illuminated area on each photodiode, it is proposed to normalize the difference between the $I_{SC}$ with the sum of the $I_{SC}$, Eq. (14). In this way, parameters that equally affect the $I_{SC}$ are simplified, such as the short-circuit current density ($J_{SC}$), due to the manufacturing of the photodiode array, and the cosine of the angle of the incident radiation. Ideally, the transfer function transitions from 0 to 1 for the desired FOV, thereby maximizing sensitivity.

$$H_{2C} = \frac{I_{sc}^A - I_{sc}^B}{I_{sc}^A + I_{sc}^B} = \frac{A_{illuminated}^A - A_{illuminated}^B}{A_{illuminated}^A + A_{illuminated}^B} \tag{14}$$

When using a square window, Eqs. (8) and (9) are substituted into Eq. (14) and a transfer function is obtained as a function of the position of the center of the light beam $L_X$, Eq. (15), which when combined with Eqs. (2), (3), and (4), results in a transfer function that depends on the zenith and azimuth angles of the incident radiation, Eq. (16). When using the circular window of radius $r$, the transfer function as a function of the position of the center of the light beam is obtained by replacing Eqs. (10) to (13) in Eq. (14), as described in Eq. (17).

$$H_{\blacksquare}(L_x) = \frac{-L_x}{r - \frac{s}{2}} \tag{15}$$

$$H_{\blacksquare}(\vartheta_i, \varphi) = \frac{h * \tan\left(\arcsin\left(\frac{n_1}{n_2}\sin\vartheta_i\right)\right) * \cos\varphi}{r - \frac{s}{2}} \tag{16}$$

## B. Simulation of the single-axis sun position sensor with two-quadrant detector

The designs were simulated to evaluate how different parameters influence the sensor performance. To simulate the designs of the single-axis sensor with a two-quadrant detector, the following design considerations were taken:

The separation between the active areas of the photodiodes, $s$, is defined based on the requirements of the technological manufacturing process of the detector. A contact of 100 µm width and 1 µm height was defined, based on the previous experience with the CSS contacts.

$$H_{\bullet}(L_x) = \frac{2\mathrm{acos}\left(\frac{L_x + \frac{s}{2}}{r}\right) - \sin\left(2\mathrm{acos}\left(\frac{L_x + \frac{s}{2}}{r}\right)\right) - 2\pi + 2\mathrm{acos}\left(\frac{L_x - \frac{s}{2}}{r}\right) - \sin\left(2\mathrm{acos}\left(\frac{L_x - \frac{s}{2}}{r}\right)\right)}{2\mathrm{acos}\left(\frac{L_x + \frac{s}{2}}{r}\right) - \sin\left(2\mathrm{acos}\left(\frac{L_x + \frac{s}{2}}{r}\right)\right) + 2\pi - 2\mathrm{acos}\left(\frac{L_x - \frac{s}{2}}{r}\right) + \sin\left(2\mathrm{acos}\left(\frac{L_x - \frac{s}{2}}{r}\right)\right)} \tag{17}$$

For the separation between the photodiodes, a barrier 150 µm wide was designed, taking as a reference the typical diffusion length of the minority carriers in a silicon photodiode (Sze, 1981 and Plá et al., 2000). The total separation between the active areas is 350 µm ($s$ = 350 µm).

For the window glass substrate, only certain thicknesses were considered because of the availability of glass substrates. In the laboratory, substrates of 1 and 2 mm thickness were available, and commercial glass wafers of 300 and 700 µm thickness were also evaluated.

To analyze how the variation impacts in the sensor response we considered the same $J_{SC}$ for both photodiodes. Differences in the order of 2% might appear in a real device $J_{SC}$ and it should be considered when simulating its response.

From the criteria taken, three experiments were planned: simulate the response of the illuminated area as a function of the window height for a given window size; simulate the response of the illuminated area, the $I_{SC}$, and the transfer function as a function of the window size for a fixed glass thickness; and analyze the response of the two-quadrant sensor by varying the zenithal and azimuthal angle of the Sun. As the sensor only detects variations in $L_X$, the first two analyzes were simplified by assuming that $L_Y$ is 0, which occurs when the azimuthal angle is 0 or 180°.

The impact of these variations in the sensitivity and linearity of the response is evaluated through linear regressions of the transfer function between 0 and 45°. The slope of the line is analyzed as the output sensitivity, and the $R^2$ value is analyzed to evaluate linearity. The results of the transfer function linear regressions are plotted with a dashed gray line.

In Fig. 6, the results of the simulation of the illuminated area of each photodiode and the transfer function as a function of the window height are shown when varying the zenithal angle of the Sun with an azimuthal angle of 0°. The four glass thicknesses were analyzed: 300 µm, 700 µm, 1 mm, and 2 mm. For the simulation, a square window of 2 mm side and a circular window of 2 mm diameter were considered.

The graph confirms the sensor's expected behavior, following the Fig. 3 reference system for the position of the light spot center in the detector plane and Fig. 5 designs. At a zenith angle of 0°, both photodiodes have an equal illuminated area, and as the zenith angle increases, the illuminated area of photodiode B decreases, while it increases in photodiode A.

The simulation results indicate that sensitivity can be improved by using thicker glass, albeit at the expense of a reduced FOV. For the square window, the sensitivity of the transfer function derived from the linear regressions increases from $4.3 \cdot 10^{-3}$ to $2.86 \cdot 10^{-2}$ 1/°. In a similar way, for the circular window, the sensitivity increases from $5.7 \cdot 10^{-3}$ to $3.19 \cdot 10^{-2}$ 1/°.

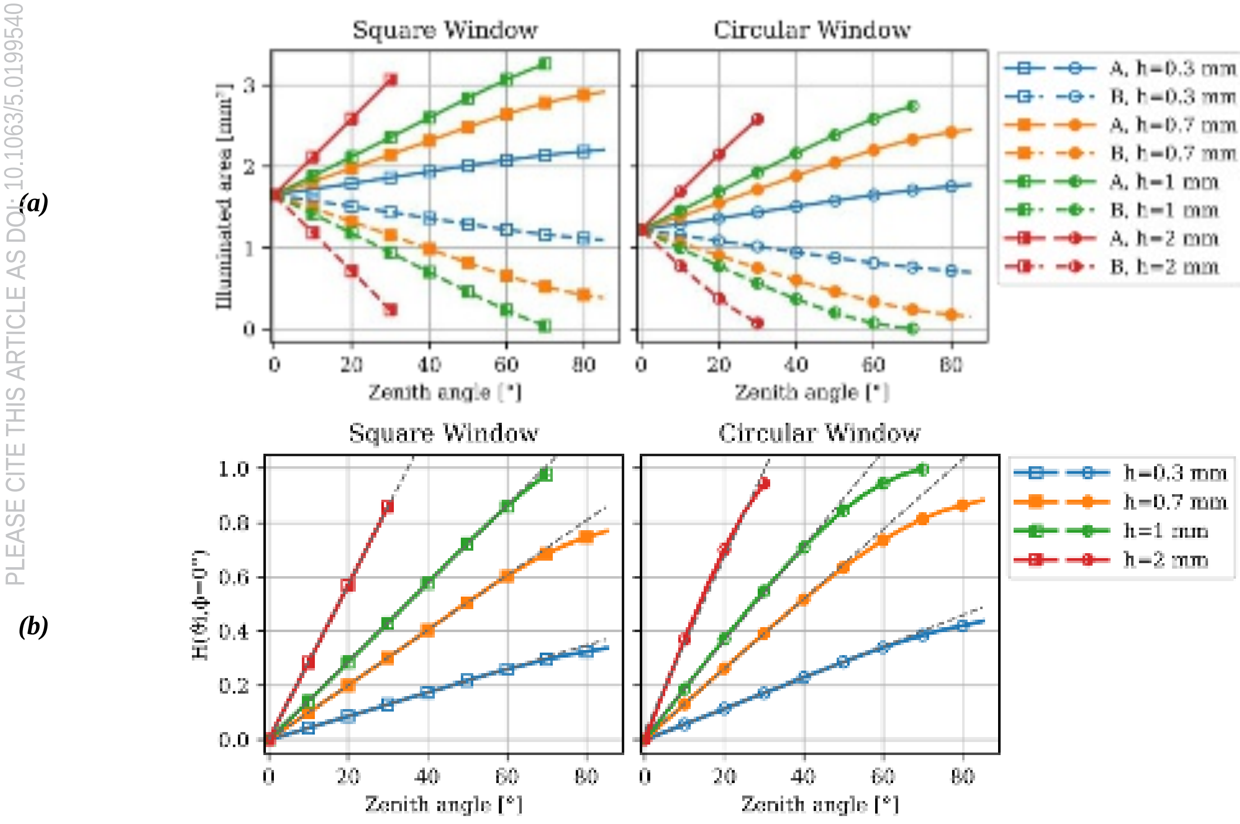


Fig. 6: Simulations performed varying the windows height, $h$, with r = 1 mm at $\varphi = 0°$, with square (left) and circular window (right). (a) Illuminated area on each photodiode. (b) Transfer function $H_{2C}$ ($\vartheta$, $\varphi = 0°$).

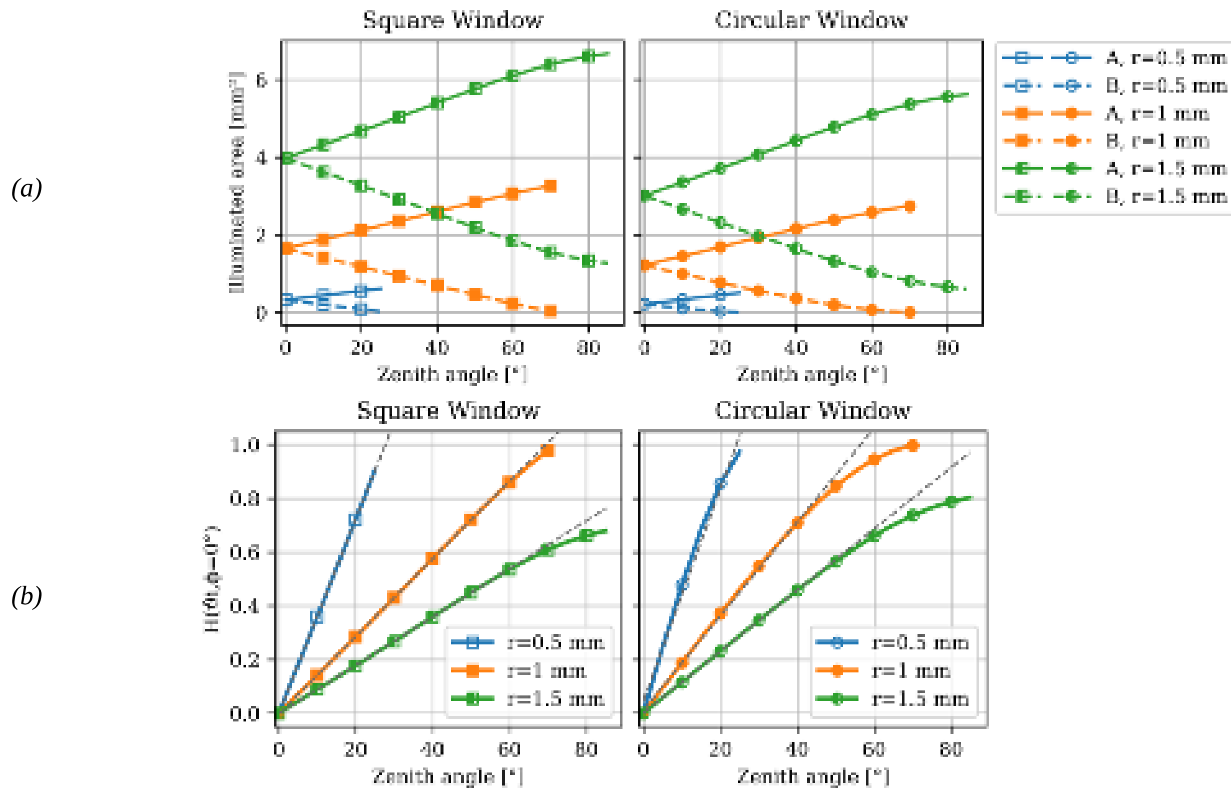


Fig. 7: Simulations performed varying the windows size ($r$), with 1 mm thick glass at $\varphi = 0°$, with square (left) and circular window (right). (a) Illuminated area as a function of the zenith angle. (b) $H_{2C}$ transfer function.

From the transfer function simulation in Fig. 6(b), it is concluded that for both window geometries, the best sensitivity is obtained with a 2 mm glass at the expense of a ±30° FOV. Instead, with the 1 mm thick glass it is obtained a FOV greater than ±60°, offering better sensitivity than the 300 and 700 µm glasses. The $R^2$ values for the square window linearization between 0 and 45° are near 1 and for the circular window are better than 0.99.

In Fig. 7 we present the simulation results of the illuminated area per photodiode, varying the windows size, with the Sun's zenith angle at 0° azimuth. The simulations were conducted for square and circular windows with sides and diameters of 1, 2, and 3 mm respectively, and a glass thickness of 1 mm. The analysis of the results indicates that the window size can limit the FOV if it approximates the separation between the photodiodes (350 µm). Additionally, altering the window size modifies the range of the illuminated area in each photodiode, which in turn affects the $I_{SC}$ range.

The simulation of the transfer function under identical conditions, Fig. 7(b), reveals that window size impacts measurement sensitivity, smaller windows lead to better sensitivity. Specifically, for square windows, the sensitivity of the transfer function obtained from the linear regressions performed increases from $9*10^{-3}$ to $3.62*10^{-2}$ 1/°. Similarly, for circular windows, the sensitivity increases from $1.14*10^{-2}$ to $3.94*10^{-2}$ 1/°. Furthermore, the sensor's transfer function exhibits greater linearity over an extended range of angles with a square window compared to a circular one. From the linear regressions performed with the data from 0 to 45°, the $R^2$ value of the transfer function linearization for the square window is close to 1, and with the circular window of r = 1 mm $R^2$ is 0.998. In Fig. 7(b) right, the model deviates from the dashed line near $\vartheta = 50°$ while for the square window it deviates at 70°.

From these comparisons we conclude that the geometry of the window is the factor that impacts the most on the linearity of the response. When analyzing the sensitivity, we conclude that by increasing the width of the window, from blue to green in Fig. 7(b), the sensitivity decreases, and by increasing the height, from blue to red in Fig. 6(b), the sensitivity increases.

Fig. 8 shows how the $I_{SC}$ varies in each photodiode for the conditions analyzed in Fig 6 y 7. With larger windows, Fig. 8(a), we observe larger illuminated areas and consequently, larger currents at $\vartheta = 0°$. As the position of the Sun changes, the illuminated area also changes, along with the angle ($\vartheta$). Eq. (1) indicates that the $I_{SC}$ is influenced by both parameters. Thus, variations in both parameters render the $I_{SC}$ curve non-trivial. Utilizing simulated $I_{SC}$ curves greatly facilitates the characterization of the fabricated sensors. It is noteworthy that, despite both windows design having the same window width $r$, the total illuminated area of circular windows is smaller than that of square windows, therefore the $I_{SC}$ range is different between geometries. On the other hand, increasing $h$ doesn't change the $I_{SC}$ at $\vartheta = 0°$, as observed in Fig. 8(b).

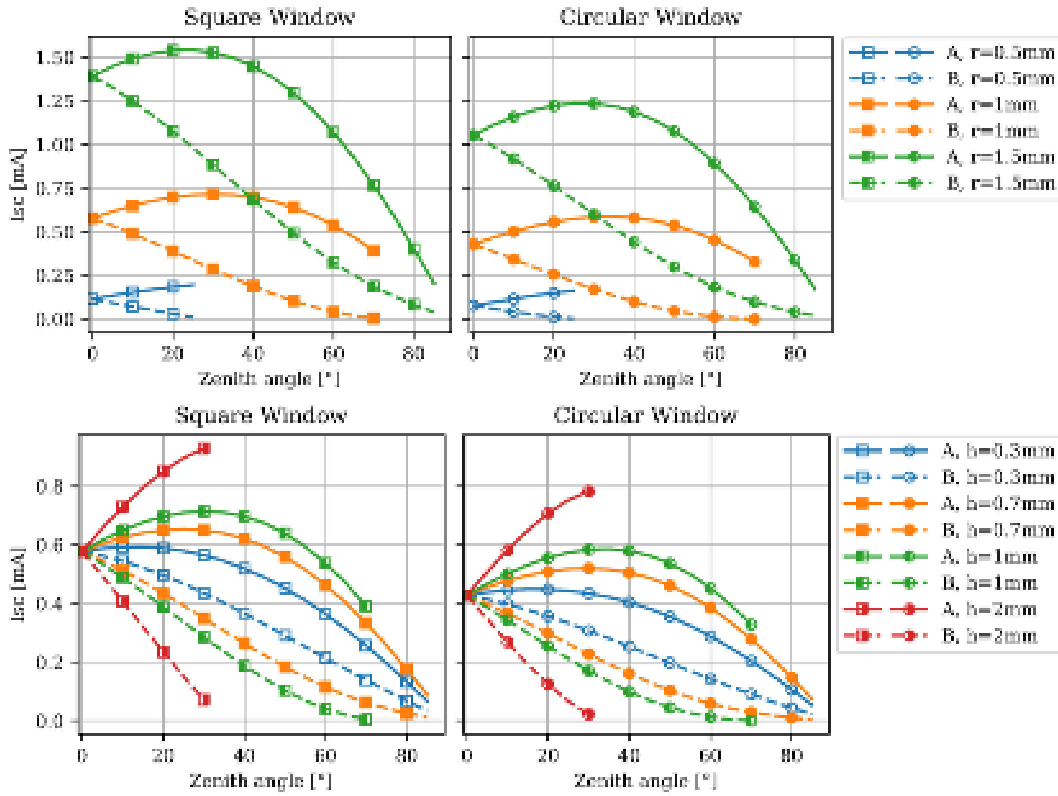


*(a)*

*(b)*

Fig. 8: $I_{SC}$ simulated for different sizes (a), height (b), and geometries of the window: square (left) and circular (right).

However, as $h$ increases for a given $\vartheta$, the difference between the output of the photodiodes also increases, this results in enhancing sensitivity.

As mentioned before, the two-quadrant detector configuration only detects variations in one axis, $L_X$, but as defined in Eq. (4), $L_X$ depends on the zenith and azimuth angles of the Sun position. For this reason, it is of interest to simulate the sensor output when varying $\vartheta_i$ and $\varphi_i$. The zenith and azimuth angles of the Sun position were varied according to Fig. 3.

For this analysis, in Fig. 9 we present the simulation of the illuminated area and transfer function of the sensor configuration depicted in Fig. 5(a), with a 2 mm side window and 1 mm glass thickness. Even though this analysis was performed for both window designs from Fig. 5(a) and (b), Fig. 9 only shows the results for the square-window sensor because, in this representation, the differences between geometries are not appreciable.

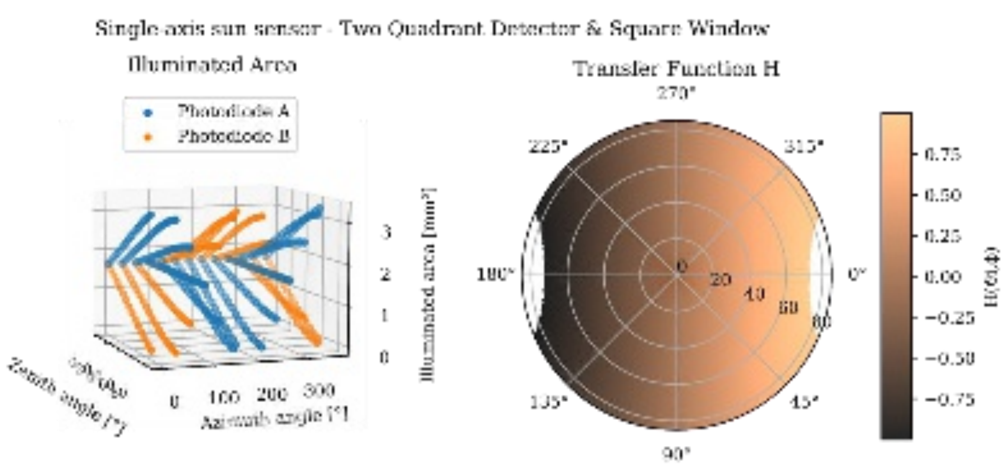


*(a)* *(b)*

Fig. 9: Simulations of the single-axis sun sensor with a two-quadrant detector and a square window with a side of 2 mm. (a) Illuminated area on each photodiode and (b) transfer function simulation, as a function of the zenith and azimuthal angles.

Fig. 9(a) shows how the illuminated area in each photodiode is affected by both angles, $\varphi_i$ and $\vartheta_i$. It is also worth noting that when the azimuth angle is increased from 0 to 90°, the difference between the illuminated areas decreases. At $\varphi$ = 90°, the illuminated areas are equal in both photodiodes and independent of $\theta$, like in a CSS, where the $I_{SC}$ only varies with the cosine of the zenith angle. As the illuminated area function is symmetric with respect to 180° of azimuth, this behavior is also observed at $\varphi$ = 270°, when the Sun azimuth is also perpendicular to the measurement axis.

In Fig. 9(b), on the other hand, the transfer function is plotted in a polar graph to examine the sensors transfer function when varying zenith and azimuth angle of the Sun. It shows that with this configuration, the sensor only provides information about the axis aligned with azimuth 0 and 180°. For a complete representation of the Sun position, it must be used two sensors measuring perpendicularly.

### C. Design of a single-axis sun position sensor with triangular and rectangular photodiodes detector

The second proposed design for the single-axis sun position sensor also employs a window to restrict incident radiation. However, the illuminated area on the detector is mainly determined by the geometry of the photodiodes.

As depicted in Fig. 10(a), the detector has two integrated photodiodes, one triangular and the other rectangular, and a rectangular window on a glass of thickness $h$. The rectangular window, with a width of $2r$, spans the detector's entire width, thereby limiting light along a single axis and uniformly illuminating a longitudinal section of the detector.

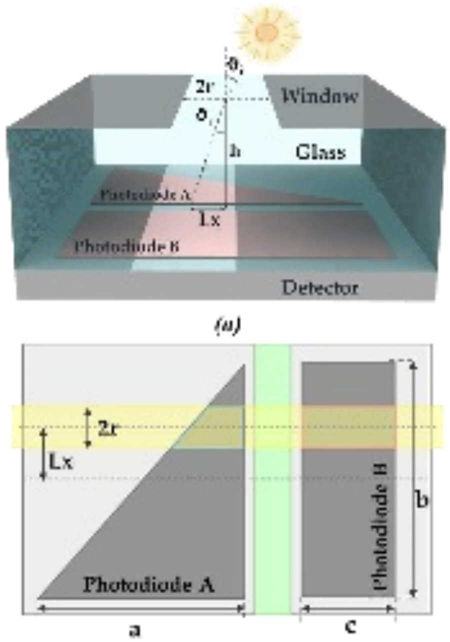


Fig. 10: (a) Single-axis position sensor design with triangular and rectangular photodiodes, (b) top view to analyze the illuminated area on the detector.

The illuminated area of the triangular photodiode varies with the zenith angle, whereas the illuminated area of the rectangular photodiode remains constant across all angles. This can be observed in Fig. 10(b), which provides a top view of the detector when illuminated at an angle $\vartheta_i$ at a given $\varphi_i$ different from 90 or 270°, when $L_X$ has a positive value.

In this setup, the maximum detection limit, Eq. (18) is determined by the point at where the border of the illuminated area aligns with the edge of the active area of both photodiodes, and the illuminated area of the rectangular photodiode is no longer constant. As inferred from Eq. (18), $L_{MAX}$ and the FOV are defined by both photodiodes height ($b$) and the width of the window ($2r$).

$$L_{x\ triangular}^{max} = \frac{b}{2} - r \tag{18}$$

The illuminated areas of the triangular (A) and rectangular (B) photodiodes are defined by Eq. (19) and Eq. (20), respectively. In these equations, $a$ represents the width of the triangular photodiode, while $c$ denotes the width of the rectangular photodiode.

$$A_A = \frac{ar}{b}(b - 2L_x) \tag{19}$$

$$A_B = c * 2r \tag{20}$$

In this design, the position of the Sun is deduced from the illuminated area on the triangular detector, and its comparison with the illuminated area on the rectangular detector. For the comparison purpose, the width of the rectangular photodiode is chosen to ensure equal illuminated area on each photodiode at $\vartheta$ = 0°. The $I_{SC}$ of the triangular photodiode is normalized with the $I_{SC}$ of the rectangular photodiode to extract the information of the illuminated area. This normalization simplifies the current density ($J_{SC}$) and its dependence on the cosine of the zenith angle. Function $H$, like Eq. (13), is proposed to ensure the transfer function yields a value between -1 and 1. The rectangular photodiode, with its constant illuminated area, serves as the reference for normalizing the sensor response. The proposed transfer function $H(L_X)$ for this design is given in Eq. (21).

$$H(L_x) = \frac{A_{illum}^A - A_{illum}^B}{A_{illum}^B} = \frac{ab - 2cb - 2aL_x}{2cb} = -\frac{2L_x}{b} \tag{21}$$

From Eq. (21), it can be inferred that both the transfer function and the sensitivity of this design remain unaffected by the window's width. Furthermore, the sensitivity exhibits an inverse proportionality to the triangular photodiode's height ($b$). When $r$ is reduced, it becomes possible to decrease $b$ without compromising the FOV. Consequently, the sensor's sensitivity can be enhanced without adversely affecting the FOV. Although the sensor sensitivity remains unaffected by the window width, it significantly defines the operational range of the $I_{SC}$. The choice of window width can be tailored to match the desired $I_{SC}$ range specific to the sensor. In this design proposal, the sensor response, and its FOV, are not influenced by the separation between the photodiodes.

### D. Simulation of the single-axis sun position sensor with triangular and rectangular photodiodes detector

The simulation analysis is conducted for the Sun at azimuths of 0 or 180° to assess the influence on the sensor response of the size of the photodiodes as well as the height and size of the window. For simulation purpose, we selected a 6 mm triangular photodiode width, considering that in the general design we said that the detector will have a total area of 12 x 12 mm$^2$ and contemplating a 1 mm contact on the outside of the photodiodes. To ensure that both photodiodes have the same illuminated area at $L_X = 0$, from Eqs. (19) and (20), the rectangular photodiode width $c$ must be half the triangular width, then $c$ = 3 mm. To determine the most suitable photodiode size for the design, three scenarios were examined: when the height of the triangle is less than, equal to, and greater than the triangle base width $a$. The simulation of the triangular photodiode illuminated area shows that when increasing $\vartheta$, at $\varphi$ = 0°, the illuminated area increases as depicted in Fig. 10(a), validating the model proposed.

Fig. 11 showcases the simulation results for different values of $b$, with a window of $h$ = 1 mm and $2r$ = 2 mm. The simulation results indicate that a triangular photodiode with a height less than its base can limit the FOV. Conversely, if the height exceeds the base, the sensitivity of the instrument diminishes. With the transfer function simulation, Fig. 11(c) we illustrate the behavior of the photodiode B as a reference. Through linear regressions, we confirmed that $H$ is linear in a FOV of 60°, considering variations in $b$. For the values analyzed, it exhibits greater linearity compared to the square window design simulated in Sec. III B. The simulation reveals that even small changes in $b$ significantly impact the sensor's sensitivity, linearity, and FOV. Reducing $b$, the sensitivity of the transfer function improves from $3*10^{-3}$ to $6.8*10^{-3}$ 1/°. However, this outcome is comparatively minor to the results obtained for the configuration of the two-quadrant detector.

An examination of the window height variation for a given window width ($2r$ = 2 mm) and photodiode size ($a = b$ = 6 mm), as shown in Fig. 12, reveals that an increase in windows height enhances the sensitivity. This observation aligns with the results obtained for the two-quadrant detector sensor.

In Fig. 13 can be seen that, as the width of the window $2r$ increases, when $a = b$ = 6 mm and $h$ =1 mm, a greater range of $I_{SC}$ is obtained in the triangular photodiode, while the transfer function is unchanged.

Following the simulations conducted, the reference values for the manufacturing parameters for this design were established. For the detector, the parameters are as follows: $a$ = 6 mm, $b$ = 3.65 mm, and $c$ = 3 mm; and for the window: $h$ = 1 mm, and $2r$ = 2 mm. Both photodiodes exhibit an $I_{SC}$ within the same range, specifically between 0 and 3 mA.

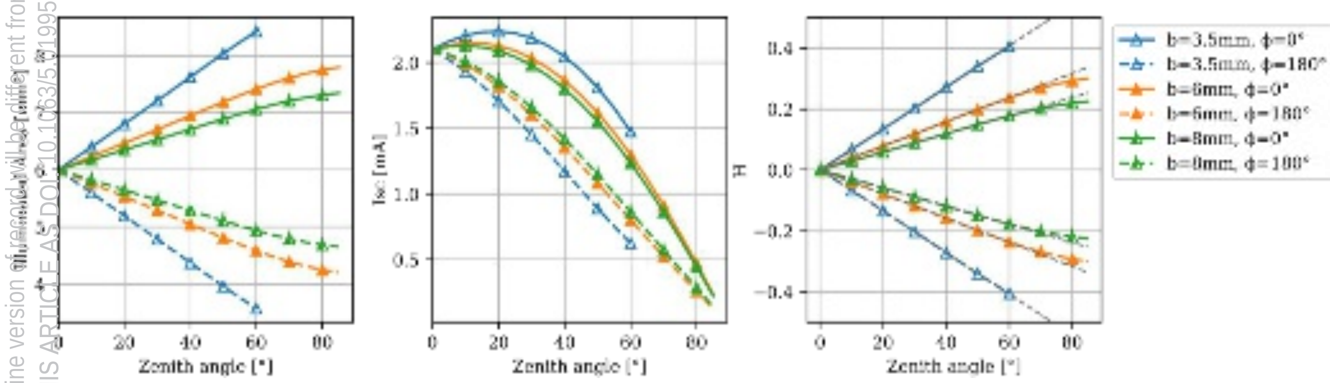


Fig. 11: Simulation of the illuminated area (left), the $I_{SC}$ (center) and transfer function $H$ (right) of the triangular photodiode for different heights of the triangle, with $a$ = 6 mm, $h$ = 1 mm, and $2r$ = 2 mm, linear regressions are plotted with grey dashed lines.

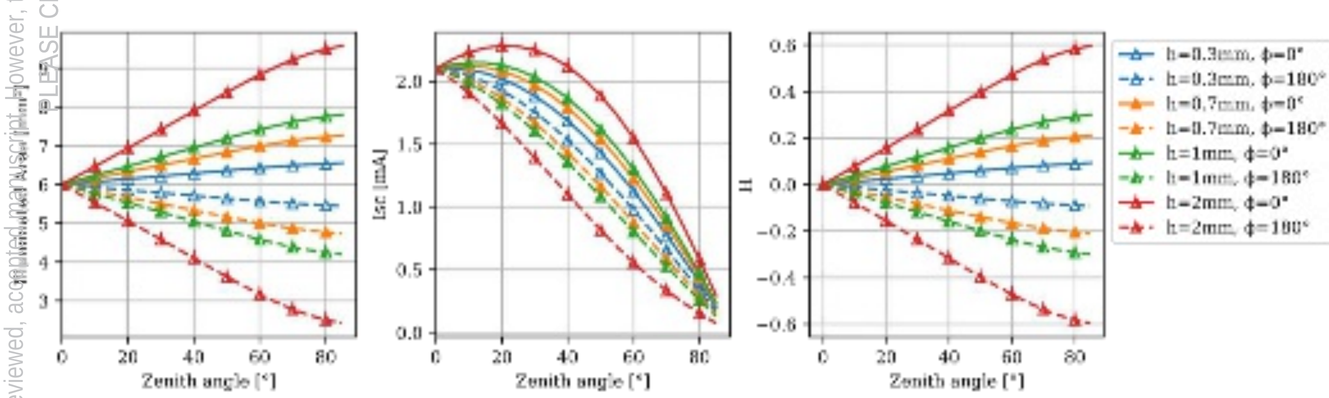


Fig. 12: Simulation of the illuminated area (left), the $I_{SC}$ (center), and transfer function $H$ (right) of the triangular photodiode for different window heights, with $a = b$ = 6 mm and $2r$ = 2 mm.

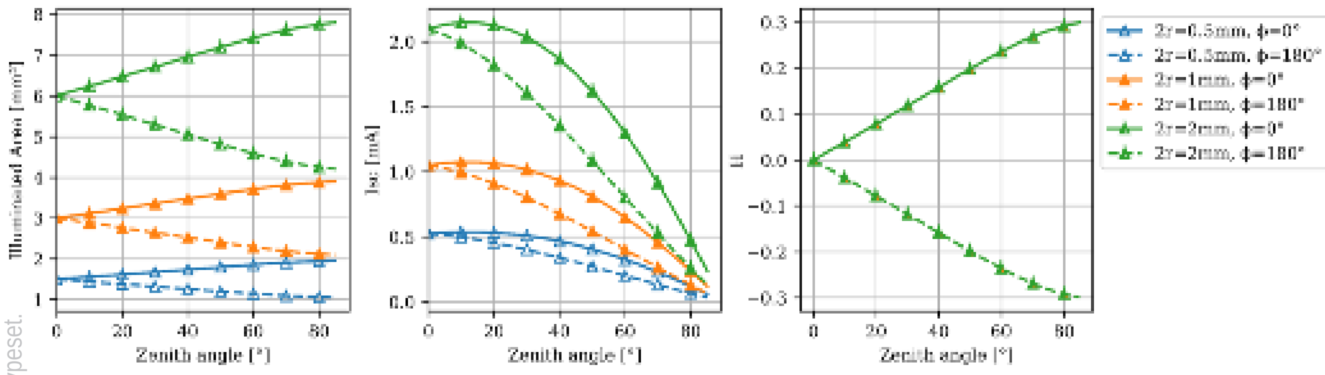


Fig. 13: Simulation of the illuminated area (left), the $I_{SC}$ (center), and transfer function (right) of the triangular photodiode for different window sizes, with $a = b = 6$ mm and $h$ =1 mm.

### E. Comparison between the designs of single-axis sun position sensors

In the concluding experiment concerning the single-axis sensor designs, a comparative analysis was conducted on the transfer function across three design proposals.

These included a two-quadrant detector equipped with a square window, a similar detector with a circular window, and a detector incorporating triangular and rectangular photodiodes. For this comparison the three configurations are under similar conditions of operation.

For this purpose, we have chosen for each configuration the same window's heigh, $h$ = 1 mm, and selected the parameters to obtain a similar $I_{SC}$ value at $\vartheta = 0°$ of approximately 0.5 mA, so the three designs have similar operational range. The simulation parameters for the two-quadrant detector sensor were established as follows: a circular window with $r$ = 1.1 mm, and a square window with $r$ = 0.95 mm. As the desired $I_{SC}$ for the triangular photodiode is lower than the analyzed in Fig. 11 simulations, we selected the narrower window simulated in Fig. 13. Consequently, smaller values for $b$ could be analyzed to improve the sensitivity without significantly reducing the FOV. After conducting simulations varying the photodiode height $b$, while considering $a$ = 6 mm, $c$ = 3 mm, $h$ = 1 mm, and $2r$ = 0.5 mm, we determined that setting $b$ to 2 mm yields optimal sensitivity within a FOV of 60°.

The comparison of the simulated illuminated area of photodiode A for each design is illustrated in Fig. 14(a), the comparison of the simulated $I_{SC}$ of one photodiode for each design is illustrated in Fig. 14(b), and the comparison of the simulated transfer function is presented in Fig. 14(c). The performance analysis for each simulated design is presented in Table I.

Table I. Performance metrics comparison.

| | Design | | |
|---|---|---|---|
| ***Parameter*** | ***Triangular*** | ***Square*** | ***Circular*** |
| *FOV [°]* | *63* | *66* | *Unobstructed* |
| *Sensitivity [1/°] (up to $\vartheta_i$ = 45°)* | *0.012* | *0.015* | *0.016* |
| *$I_{SC}$ (0°) [mA]* | *0.525* | *0.515* | *0.531* |
| *$I_{SC}^{MAX}$ [mA]* | *0.616* | *0.65* | *0.696* |

Upon comparison, it is discerned that both architectures, the one equipped with a square window and the one with the triangular photodiode exhibit a linear response. Conversely, the sensor featuring a circular window demonstrates slightly better sensitivity in a FOV of 45°. However, the design incorporating a triangular photodiode offers a lower sensitivity than the two-quadrant configuration under similar conditions.

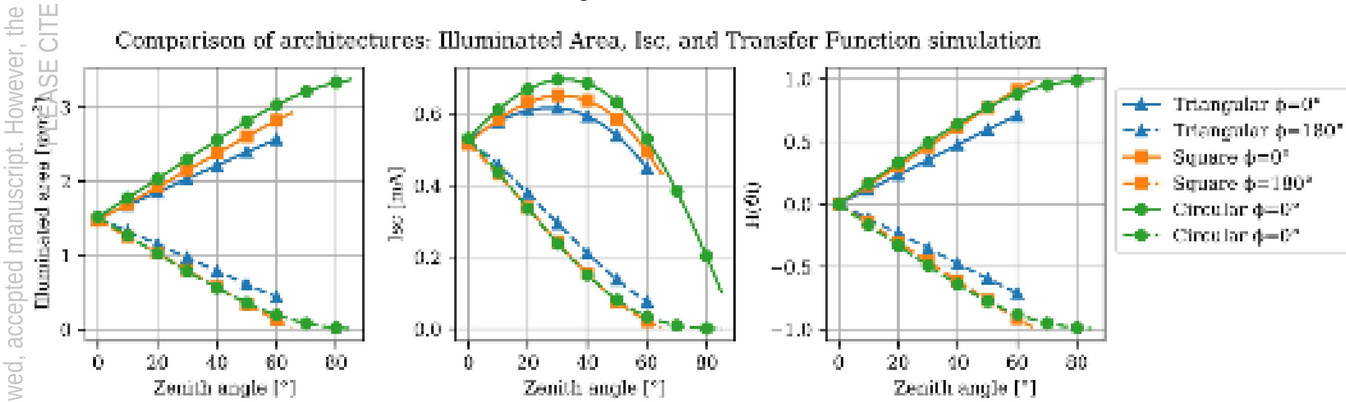


*(a)* *(b)* *(c)*

Fig. 14: Simulation comparison of the three proposed designs with a glass of 1 mm thick. (a) illuminated area of photodiode A of each design, (b) $I_{SC}$ of one photodiode of each design, and (c) transfer function of the three proposed designs.

We concluded that the transfer function linearity is determined by the window or photodiode geometry.

As the window width is smaller for the square design than for the circular window to comply with the $I_{SC}$ requirement, the calculated FOV is also smaller. For the circular window an unobstructed FOV is predicted, however, the transfer function shows a big loss of sensitivity for angles over $\vartheta_i = 60°$. This serves as an example that the effective FOV of the sensors is not always as large as initially predicted and it must be analyzed in each case.

For the circular window, the sensitivity could be improved because of its geometry, for smaller angles the difference between the illuminated area of each photodiode is bigger than for the larger angles, and the total illuminated area is not constant, it increases as $L_X$ increases. On the contrary, with the square window, the total illuminated area is constant and the difference between the illuminated areas is defined by a linear function.

The circular window will have an advantage over the square window for the alignment between window and detector as it must be considered the misalignment with respect to x and y axes, but for the square windows it also must be considered an angular misalignment, which will modify the geometry of the illuminated area on each photodiode and the measured transfer function.

## IV. DUAL-AXIS SUN POSITION SENSOR

To obtain the position of the Sun within a three-dimensional representation, comprising zenith and azimuth angles, a detector sensitive to both $L_X$ and $L_Y$ is required. A sensor capable of determining both zenith and azimuth angles is referred to as a dual-axis position sensor. The designs proposed for the dual-axis measurement operate on the same principle as the single-axis sensors: they consist of a photovoltaic detector and a window separated with a glass, which directs light towards a specific region of the detector based on the position of the Sun. Based on the designs of the single-axis sensors, two architectures or configurations are proposed to measure in two axes.

The first configuration comprises a detector with an array of four photodiodes, arranged into four quadrants. This arrangement yields two perpendicular single-axis sensors, each consisting of two quadrants. Both a square and a circular window were modeled for this configuration, and simulations were conducted to evaluate how the geometry of the window impacts the dual-axis sensor's response. The second configuration is based on the single-axis sensor with a triangular photodiode and a rectangular reference photodiode. A third photodiode was added for measurement along the other axis, and the window's geometry was altered. Consequently, the detector consists of an array of three photodiodes: one for each axis and a common reference for both axes.

### A. Design of dual-axis sun position sensor with four-quadrant detector

The design of a sensor equipped with a four-quadrant detector is illustrated in Fig. 15, with a square and circular window.

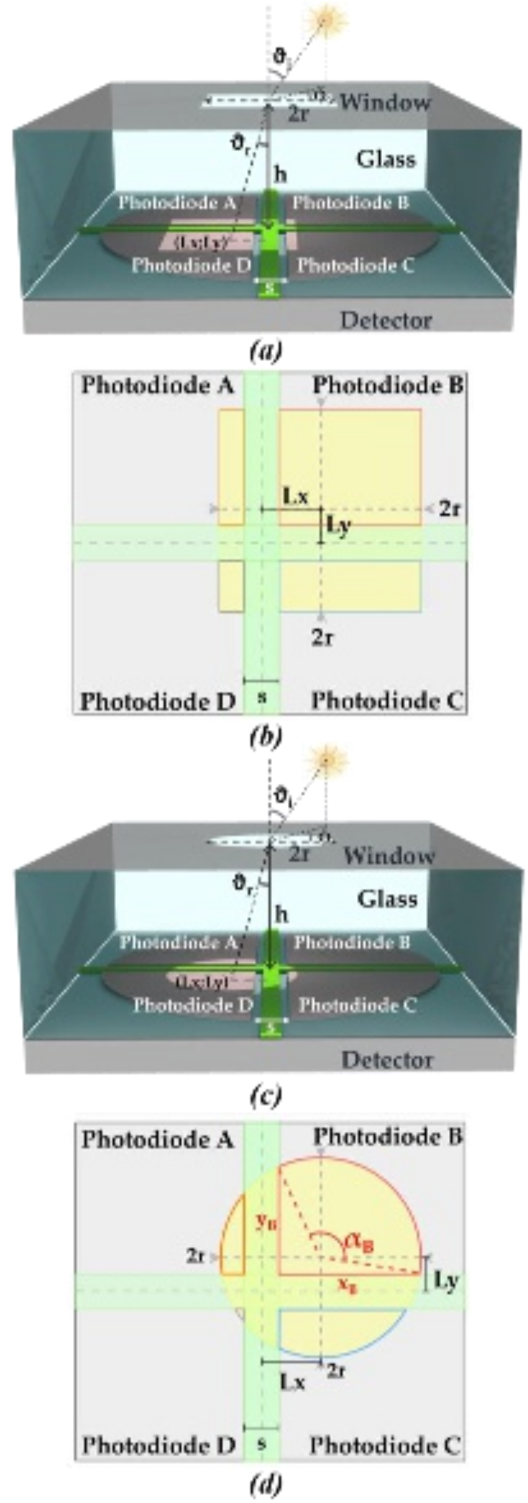


Fig. 15. Design of the dual-axis sun position sensor with four-quadrant detector and its top view relative to the window geometry, *a* and *b*, square window, *c* and *d*, circular window.

$$H(L_X) = \frac{(I_{sc}^A + I_{sc}^D) - (I_{sc}^B + I_{sc}^C)}{I_{sc}^A + I_{sc}^B + I_{sc}^C + I_{sc}^D} = \frac{(A_{illum}^A + A_{illum}^D) - (A_{illum}^B + A_{illum}^C)}{A_{illum}^A + A_{illum}^B + A_{illum}^C + A_{illum}^D} \tag{22}$$

$$H(L_Y) = \frac{(I_{sc}^A + I_{sc}^B) - (I_{sc}^C + I_{sc}^D)}{I_{sc}^A + I_{sc}^B + I_{sc}^C + I_{sc}^D} = \frac{(A_{illum}^A + A_{illum}^B) - (A_{illum}^C + A_{illum}^D)}{A_{illum}^A + A_{illum}^B + A_{illum}^C + A_{illum}^D} \tag{23}$$

In Fig. 15(a), the sensor features a square window with a side length of *2r*. While in Fig. 15(c), it is depicted an alternative design with a circular window of diameter *2r*. The sensor design incorporates a matrix of four photodiodes integrated on a silicon substrate, separated by two $SiO_2$ barriers each one of 150 µm width.

The center of the window is aligned with the matrix center, ensuring that at a zenith angle of 0°, the illuminated area is equally distributed across all four photodiodes. Fig. 15(b) and 15(d) provide a top-down view of the illuminated detector when both $L_X$ and $L_Y$ are positive, facilitating an analysis of the illuminated area within each photodiode relative to the window geometry. The position of the light spot center ($L_X$, $L_Y$) depends on the zenith and azimuth angles of the Sun, Eq. (3) to (5).

Given that the photodiodes are arranged into four quadrants, it is possible to propose two transfer functions, $H(L_X)$ and $H(L_Y)$. These functions are analogous to Eq. (14) from the single-axis sensor with two quadrants detector. The photodiodes relevant to each axis are grouped in accordance with Eqs. (22) and (23).

In the case of the square window, the illuminated area in each photodiode is modeled as the area of the rectangle determined by Eqs. (24) to (27).

$$A_A = \left(r - L_X - \frac{s}{2}\right)\left(r + L_Y - \frac{s}{2}\right) \tag{24}$$

$$A_B = \left(r + L_X - \frac{s}{2}\right)\left(r + L_Y - \frac{s}{2}\right) \tag{25}$$

$$A_C = \left(r + L_X - \frac{s}{2}\right)\left(r - L_Y - \frac{s}{2}\right) \tag{26}$$

$$A_D = \left(r - L_X - \frac{s}{2}\right)\left(r - L_Y - \frac{s}{2}\right) \tag{27}$$

When a circular window is employed, Fig. 15(d), the illuminated area in each photodiode constitutes a portion of the circular spotlight. Each circular portion can be divided into a triangle, formed by the *x* and *y* sides, and the circular segment that corresponds to the central angle alpha ($\alpha$), as outlined in Eq. (28). In this context, the letter *i* denotes each individual photodiode. The central angle $\alpha$ corresponding to each photodiode is calculated according to Eq. (29), using the triangle hypotenuse as the circular segment chord.

$$A_i = \frac{x_i * y_i}{2} + \frac{1}{2} r^2 (\alpha_i - sin(\alpha_i)) \tag{28}$$

$$\alpha_i = 2 * arcsin\left(\frac{\sqrt{x_i^2 + y_i^2}}{2r}\right) \tag{29}$$

The *x* and *y* sides of the illuminated area of each photodiode are calculated according to Eqs. (30) to (37). For this model we used the equation of a circle centered in ($L_X$, $L_Y$) in the detector plane reference system from Fig. 3.

$$x_A = \sqrt{(r^2 - \left(\frac{s}{2} - L_Y\right)^2} - L_X - \frac{s}{2} \tag{30}$$

$$y_A = \sqrt{(r^2 - \left(-\frac{s}{2} - L_X\right)^2} + L_Y - \frac{s}{2} \tag{31}$$

$$x_B = \sqrt{(r^2 - \left(\frac{s}{2} - L_Y\right)^2} + L_X - \frac{s}{2} \tag{32}$$

$$y_B = \sqrt{(r^2 - \left(\frac{s}{2} - L_X\right)^2} + L_Y - \frac{s}{2} \tag{33}$$

$$x_C = \sqrt{(r^2 - \left(-\frac{s}{2} - L_Y\right)^2} + L_X - \frac{s}{2} \tag{34}$$

$$y_C = \sqrt{(r^2 - \left(\frac{s}{2} - L_X\right)^2} - L_Y - \frac{s}{2} \tag{35}$$

$$x_D = \sqrt{(r^2 - \left(-\frac{s}{2} - L_Y\right)^2} - L_X - \frac{s}{2} \tag{36}$$

$$y_D = \sqrt{(r^2 - \left(-\frac{s}{2} - L_X\right)^2} - L_Y - \frac{s}{2} \tag{37}$$

In this setup with a circular window, on each axis, $L_{MAX}$ is determined by Eq. (38). The criterion for $L_{MAX}$ is that the combined illuminated area of two neighboring photodiodes exceeds zero. This arrangement underscores the importance of closely integrating the photodiodes to prevent any impact on the FOV of the sensor.

$$L_{X,Y\ 4C\bullet}^{MAX} = \sqrt{r^2 - \left(\frac{s}{2}\right)^2} - \frac{s}{2} \tag{38}$$

As a practical consideration to prevent the size of the photodiodes from limiting the FOV and to ensure the validity of the model, it is requirement that the active area of each photodiode exceeds the maximum illuminated area calculated.

### B. Simulation of the dual-axis sun position sensor with a four-quadrant detector

The simulation of the dual-axis position sensor, equipped with a four-quadrant detector, is based on the design principles of the single-axis sensor. The parameters such as window size, glass thickness, and photodiode separation are consistent with those of the single-axis sensor with a two-quadrant detector and are listed in Table II. Upon defining the manufacturing parameters for the sensors, it becomes pertinent to establish an ideal curve that depicts the $I_{SC}$ behavior of each photodiode in relation to the position of the Sun. This ideal response will enable an analysis of the performance of the manufactured devices as well as adjust parameters as a function of the desired current range of the sensor. To achieve this, two experiments were conceived. The first aims to validate, through simulation, the proposed model of the illuminated area in each photodiode. The second experiment intends to simulate the $I_{SC}$ of each photodiode and the sensor transfer function.

Table II. Parameters considered in the simulations.

| *Parameter* | *Symbol* | *Value* |
|---|---|---|
| *Glass thickness [mm]* | *h* | *1* |
| *Window width [mm]* | *r* | *1* |
| *Active area separation [mm]* | *s* | *0.35* |
| *Short-circuit current density at AM0 [mA/mm²]* | $J_{SC}$ | *0.35* |

The result of the first experiment is shown in Fig. 16. It confirms that the model representing the illuminated area in each photodiode as a function of the Sun position, exhibits the desired behavior. At a zenith angle of 0°, all photodiodes have an equal illuminated area, and as the zenith angle changes, the most illuminated photodiode varies depending on the azimuthal angle.

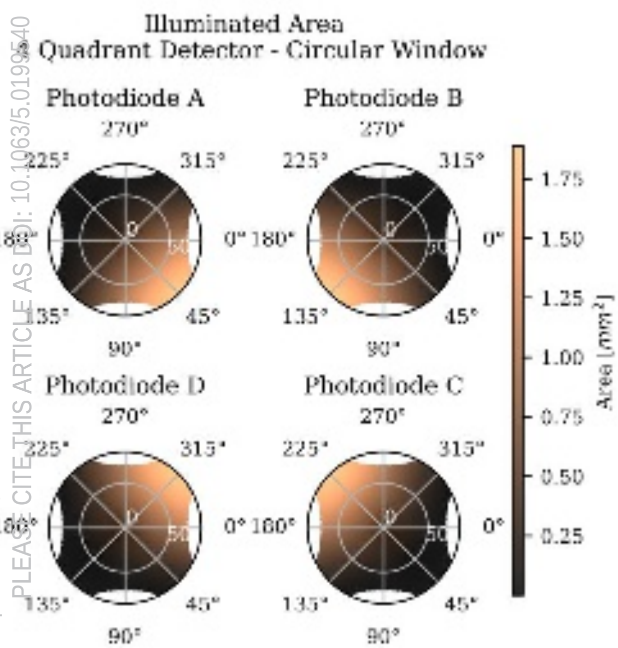


Fig. 16: Simulation of the illuminated area on each photodiode as a function of the position of the Sun when using a circular window.

To validate the four-quadrant detector configuration model, we analyzed the variations in the illuminated areas. For each photodiode, the illuminated area is equal at zenith angle 0°, and it reaches maximum when the Sun's azimuth is diagonally positioned relative to the quadrant where the photodiode is situated, as depicted in Fig. 15(c) with reference to Fig. 3 representation of the Sun position. Furthermore, with the Sun positioned at $\varphi$ = 45° as shown in Fig. 16, photodiode A exhibits the largest illuminated area.

The second simulation (Fig. 17) yields the range of the $I_{SC}$, identifying the position of the Sun at which the current reaches its peak. This is a crucial first step in sensor characterization. As depicted in Fig. 17, the maximum $I_{SC}$ value is 0.87 mA, and it is observed at a zenith angle of 44° and azimuth angles of 45°, 135°, 225°, and 315° for photodiodes A, B, C, and D, respectively, as denoted with a red dot in Fig. 17. Although the simulation with the square window is not shown, when a square window is employed, the maximum $I_{SC}$ is obtained at a zenith angle of 40°, with a value of 1 mA.

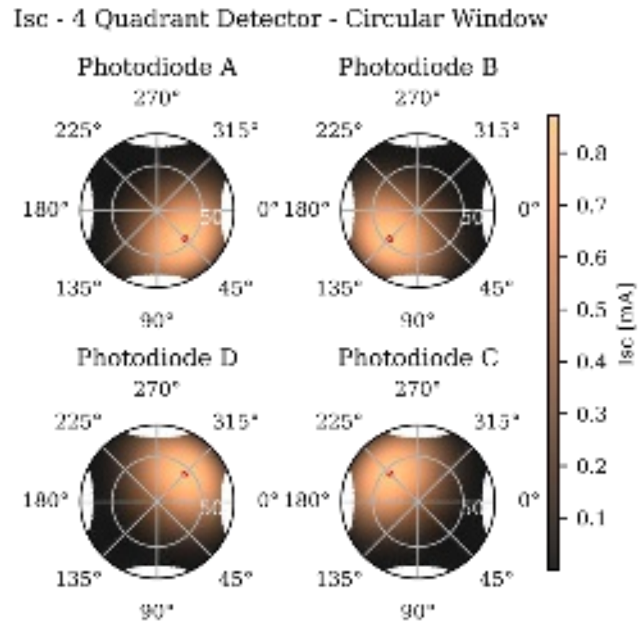


Fig. 17: $I_{SC}$ simulation of each photodiode of the sensor with a four-quadrant detector and a circular window as a function of the position of the Sun.

The simulations of the transfer functions are shown in Fig. 18 in a polar graph. Each function varies between -1 and 1 and it depends only on the measurement axis. It is proposed to determine the position of the Sun by following the subsequent steps: from the $I_{SC}$ of each photodiode, compute $H$ to derive $L_X$ and $L_Y$, and finally, calculate the zenith and azimuth angles based on $L_X$ and $L_Y$.

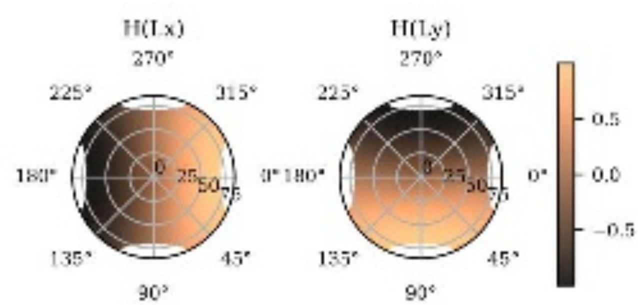


Fig. 18: Transfer function ($H_{4C}$) simulation for each axis of a sensor with a four-quadrant detector and a circular window.

### C. Dual-axis sun position sensor based on a triangular photodiode

The design under consideration, to measure the Sun position in two axes, extends the concept of the single-axis sensor equipped with a triangular photodiode. This extension involves the addition of a third rectangular photodiode to facilitate measurement in the second axis, as depicted in Fig. 19(a). The illuminated area within the added photodiode is dictated by the geometry of the window, as illustrated in Fig. 19(b). The latter configuration is similar to that of the two-quadrant detector with a square window.

To achieve the independent measure of both axes, a window was engineered to uniformly illuminate the cross-sections of photodiodes A and B. However, the window does not span the entire length of the detector. Consequently, at a zenith angle of 0°, the edge of the window aligns with the center of the rectangular detector.

In this design, photodiode B serves as a reference for both axes. When the position of the Sun implies variations in $L_X$, the illuminated area of photodiode A will change, and when it implies variations in $L_Y$, the illuminated area in photodiode C will change.

The modifications introduced in this design are that $L_Y^{MAX}$ is defined by Eq. (39) and the illuminated area on photodiode C is defined according to Eq. (40).

$$L_y^{max} = \frac{d}{2} \tag{39}$$

$$A_{illum}^{C} = 2r * \left(\frac{d}{2} + Ly\right) \tag{40}$$

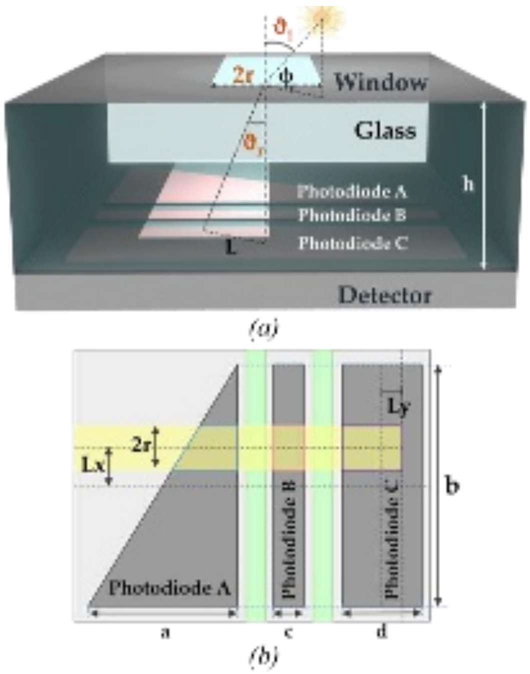


Fig. 19: (a) Design of the dual-axis sun position sensor with a triangular photodiode and rectangular window. (b) Top view to analyze the illuminated area on the detector.

The transfer function $H$ for the second axis measurement responds to Eq. (41).

$$H(L_y) = \frac{I_{sc}^{C} - I_{sc}^{B}}{I_{sc}^{B}} = \frac{d}{2c} + \frac{L_y}{c} - 1 = \frac{2L_y}{a} \tag{41}$$

To achieve a transfer function that is 0 when $\vartheta = 0°$, we need to choose a value for $d$ such that Eq. (41) equals 0 when $L_Y$ is 0. Consequently, $d$ must be equal to $2c$. Since $c$ should be $a/2$ to ensure similar conditions for $H(L_X)$ (as discussed in Sec. III D), photodiodes A and B must have identical widths. The transfer function for both axes will exhibit symmetry if $a$ and $b$ share the same dimensions.

The sensitivity of the $x$-axis will be defined by $b$, and for $y$-axis, it will be defined by $a$. In this design the FOV of the sensor will be defined independently for each measurement axis as reckoned from Eq. (18) and (39).

Analogous to the single-axis sensor, the separation between photodiodes in this configuration does not impact on sensor the response. In contrast to the four-quadrant setup, this sensor architecture features only three photodiodes.

### D. Simulation of the dual-axis sun position sensor based on a triangular photodiode

To simulate the sensor output some considerations were taken, considering the observations made in the model. To obtain a detector with a size of 12 x 12 mm, we selected a 2 mm triangular photodiode width, and with the model considerations, the reference photodiode has 1 mm width, and the rectangular photodiode C width ($d$) is also 2 mm. To obtain the same sensitivity in both axes, we simulate a detector configuration where $a$ and $b$ have the same length. For other combinations, sensitivity may improve in the $x$-axis but will differ from $y$-axis. The simulations were performed considering that $2r = 0.5$ mm and $h = 1$ mm.

The simulation of the transfer function for each axis is presented in Fig. 20. We can observe that the FOV is not symmetrical for $H_X$ and $H_Y$. A smaller $r$ will result in larger FOV for the triangular photodiode, but with a smaller range of the current outputs. The window width only limits the FOV of the $x$-axis, for $y$-axis it is defined by the photodiode C width. To analyze the sensitivity and FOV, we made a comparison of the transfer function of each axis in the same graph (Fig. 21).

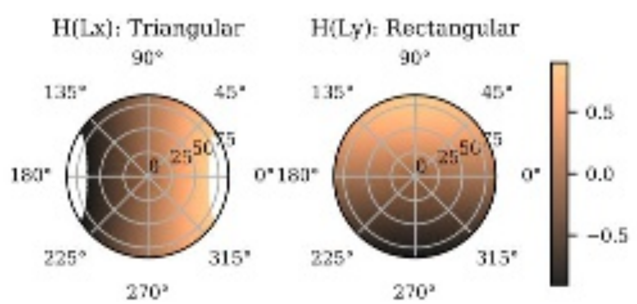


Fig. 20: Transfer function ($H_X$, $H_Y$) simulation of the dual axis sun sensor with triangular photodiode.

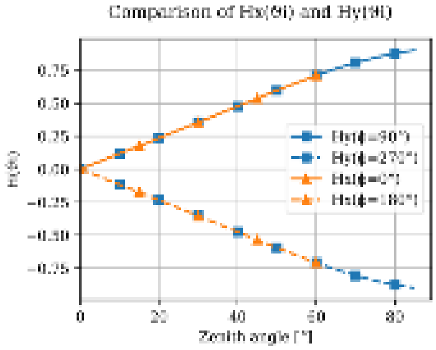


Fig. 21: Comparison of the transfer function ($H_X$, $H_Y$) simulation of the dual axis sun sensor with triangular photodiode.

From Fig. 21 we can conclude that the transfer function is linear in a 60° FOV for both axes, it agrees with the results obtained in the simulations of Sec. II B for the square window geometry and Sec. III D. Fig 22 shows the simulated $I_{SC}$ considering a $J_{SC}$ of 35 mA/cm$^2$.

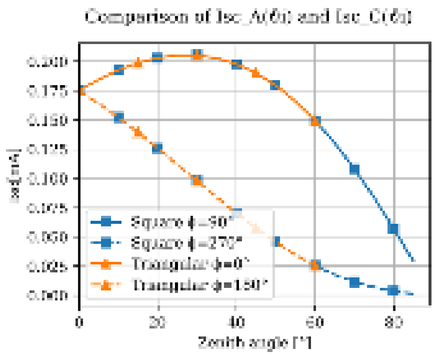


Fig. 22: Comparison of the $I_{SC}$ simulation of triangular photodiodes A (triangular) and C (square), with $a = b = d = 2$ mm and $2r = 0.5$ mm.

## V. CONCLUSIONS

This study describes the design methodology of sun position sensors, introducing various architectures within a shared operational principle, an array of photodiodes where the illuminated area is proportional to the position of the Sun. These architectures were conceived to enhance performance and comply with the existing manufacturing capabilities at CNEA. The design process involved choosing the sensor architecture, modeling its output, and then evaluating the model through simulation. To simulate the response of the models a program was developed in Python and the sensitivity and linearity was evaluated through linear regressions.

From the simulations performed we concluded that within each design, the key factors that influence the sensitivity and FOV performance are the window height and size, as well as the photodiode size, depending on the sensor architecture.

We concluded that in general, larger windows imply larger illuminated areas, thereby diminishing the significance of minor fluctuations in Sun positioning as they represent a smaller proportion of the overall area. Consequently, such configurations exhibit a reduced sensitivity. This analysis was performed for a given glass thickness. We also concluded, when varying the window height, that the thicker the glass, the greater the sensitivity of the response. On the other hand, the FOV is determined by the height and width of the window, and the size and position of the photodiodes in the detector plane.

When comparing detectors geometries, we concluded that in the triangular photodiode detector, the detector's geometry determines the illuminated area thus greatly influencing sensor performance. Specifically, the aspect ratio of the triangular photodiode defines the sensitivity while the triangle height defines the FOV. In contrast, the geometry of the two and four-quadrant detectors does not affect the sensor performance, as the illuminated area is defined by the window geometry. In this configuration, only the separation between photodiodes has implications for the FOV.

From the comparison across architectures, for the same conditions of operation, it was concluded that the sensor with the two-quadrant detector configuration offers a better sensitivity than the one with a triangular photodiode. And that the combination of the two-quadrant detector with a circular window demonstrates better sensitivity in a FOV of 45° than with a square window.

We also concluded that the sensor component that defines the illuminated area pattern on the photodiodes is the one that defines the linearity of the response, for the two-quadrant detector it is the geometry of the window. For a better linearity of the output a square window is preferred. However, despite its reduced linearity, the circular window is a more suitable option compared to the square window. This preference is justified by its superior sensitivity and the additional benefit of symmetry, which has the potential to effectively mitigate alignment errors. Though, the design incorporating triangular and rectangular photodiodes offers a technological advantage, as the response remains unaffected by the separation between photodiodes. When comparing our reported sensitivity values with previews work by (Boslooper et al., 2012), we concluded that our results are in the same order of magnitude.

A practical observation about the transfer function is that it ideally transitions from 0 to 1 for the desired FOV. This implies that the sensor is non-responsive outside the desired FOV and fully responsive within it, thereby maximizing the sensitivity within the desired viewing range. Consequently, we can calculate the maximum sensitivity achievable by the sensor within a specific FOV.

The single-axis sensor designs were extrapolated to a dual-axis sensor, capable of ascertaining both the zenith and azimuth angles of the Sun. From the results obtained it was concluded that the desired response of the sensor must have a linear output, with good sensitivity in a FOV of at least 45°.

This comparative study has proven to be an important tool that improves the decision-making process when developing new products for space applications. This analysis primarily contributes to define the manufacturing parameters and response characteristics of the position sensors slated for production in the DES. The specific manufacturing parameters such as separation between photodiodes, contacts width, and total area of the detector of the sensors were determined based on the experience of manufacturing CSS, and the available technology at CNEA. The other manufacturing parameters such as active area of the photodiodes, the windows size, and the glass thickness are defined by the simulation results.

The results obtained from the modeling can be used to get the Sun's position when the sensor is operative. Upon manufacturing the sensors, it is proposed to ascertain the Sun's position by adhering to the following steps: measure the $I_{SC}$ of each photodiode, compute $H$ to derive $L_X$ and $L_Y$, and finally, calculate the zenith and azimuthal angles based on $L_X$ and $L_Y$. The proposed models will serve as evaluative tools of the response of the manufactured sensors, as it has proven to be useful for detection and determination of alignment errors during the characterization of elaborated prototypes.

The designs presented are the first step in the development process of nationally manufactured sun position sensors to obtain a dual-axis representation of the position of the Sun, that will be used as a complement to the existing CSS as part of the ADCS of a satellite. In this sense, the next steps involve studies on radiation damage, thermal cycling, and mechanical testing. The development of these sensors in Argentina will allow the use of instruments adapted to the specific needs requested from each space mission, contributing to the Argentinian National Space Plan.

This study also contributes to other lines of work of CNEA, such as terrestrial solar trackers for measurement and characterization of solar radiation for applications in reference solar cell calibration.

## VI. REFERENCES


Alurralde, M., Barrera, M., Bolzi, C.G., Bruno, C.J., Cabot, P., Carella, E., Di Santo, J., Durán, J.C., Fernández Slezak, D., Fernández Vázquez, J., Filevich, A., et al., "Development of solar arrays for Argentine satellite missions", Aerospace Science and Technology, 26(1), 38-52 (2013).

Antonello A., Olivieri L., and Francesconi A., "Development of a low-cost sun sensor for nanosatellites", Acta Astronautica, 144, 429-436, (2018).

Bastida, L.A., Barral, F., Videla, M. E., Sambrano, E., and Plá, J.C., "Prototipo de concentrador solar para aplicaciones en CPV", Avances En Energías Renovables Y Medio Ambiente-AVERMA, 26, 249–261 (2022).

Bogado, M., Tamasi, M. J L, Bolzi, C., and Raggio, D., "Desarrollo de sensores solares en argentina, aplicaciones terrestres y espaciales", Revista Brasileira de Energia Solar, 6(1) (2015).

Bolzi, C. G., Bruno, C. J., Durán, J. C., Godfrin, E. M., Bogado, M. M., Merino, L., Tamasi, M., and Barrera, M., "First experiment of Argentine solar cells in space: modules fabrication, characterisation, and telemetry data analysis from SAC-A satellite", Solar Energy Materials and Solar Cells, 73(3), 269-280 (2002).

Bolzi, C. G., Martínez Bogado, M. G., and Tamasi, M.J.L., "Reseña del desarrollo de sensores solares en CNEA para satelitales", Energías Renovables y Medio Ambiente, 31, 2684-0073 (2013).

Boslooper, E., van der Heiden, N., Naron, D., Schmits, R., van der Velde, J.J., and van Wakeren, J., "BepiColombo Fine Sun Sensor", Boslooper: ESA and CNES, International Conference on Space Optics - ICSO 2012, 10564 (2012).

Buonocore, M., Grassi, M., and Rufino, G., "Aps-based miniature sun sensor for earth observation nanosatellites", Acta Astronautica, 56 (1–2), 139-145, (2005).

Celebi, M., and Gulmammadov, F., "Modeling and Simulation Activities for Digital Sun Sensor Development", AIAA Modeling and Simulation Technologies Conference, 1438 (2016).

Diriker, F.K., Frias, A., Keum, K.H., and Lee, R.S.K., "Improved Accuracy of a Single-Slit Digital Sun Sensor Design for CubeSat Application Using Sub-Pixel Interpolation", Sensors 21, 1472, (2021).

Gröbner J., and Kouremeti N., "The Precision Solar Spectroradiometer (PSR) for direct solar irradiance measurements", Solar Energy (185) 199-210 (2019).

Jamroen, C., Fongkerd, C., Krongpha, W., Komkum, P., Pirayawaraporn, A., Chindakham, N., "A novel UV sensor-based dual-axis solar tracking system: Implementation and performance analysis", Applied Energy, 299, 117295 (2021).

Kim, H. J., "A Sun-Tracking CMOS Image Sensor With Black-Sun Readout Scheme," IEEE Transactions on Electron Devices, 68(3), 1115-1120, (2021).

Leijtens, J., Broekmans, D., Stelwagen, F., "Digital Sunsensors, where there is no ease, in adding ten degrees," Proc. SPIE, International Conference on Space Optics — ICSO, 11852 (2021)

Plá J.C., Tamasi M.J.L., Bolzi C.G., Venier G.L., and Durán J.C., "Short circuit current vs cell thickness in solar cells under rear illumination: a direct evaluation of the diffusion length", Solid-State Electronics, 44(4), 719-724, (2000).

Pereira, N., Bolsée, D., Sluse, D., Michel, A., Meftah, M., Damé, L., and Irbah, A., "Design of an optical sun sensor for a space application: a reliable passive sun tracking device for the SOLAR/SOLSPEC instrument", Optical Sensors 2017,10231, 339-346 (2017).

Romijn, J., Vollebregt, S., de Bie, V. G., Middelburg, L. M., El Mansouri, B., van Zeijl, H. W, May, A., Erlbacher, T., Leijtens, J., Zhang G., Sarro P., "Microfabricated albedo insensitive sun position sensor system in silicon carbide

with integrated 3D optics and CMOS electronics", Sensors and Actuators A: Physical, 354, 114268, (2023).
Salgado-Conrado, L., "A review on sun position sensors used in solar applications", Renewable and Sustainable Energy Reviews", 82(3), 2128-2146 (2018).
Smets, A., Jäger, K., Isabella, O., Swaaij, R. V., and Zeman, M. "Solar Energy: The Physics and Engineering of Photovoltaic Conversion, Technologies and Systems", UIT Cambridge, (2016).
Sze, S. M., "Physics of semiconductor devices. 2nd Edition", John Wiley & Sons, (1981).
Wei, M.S., Xing, F., Li B., and You Wei Z, "Investigation of Digital Sun Sensor Technology with an N-Shaped Slit Mask", Sensors, 11, 9764-9777 (2011).
Yost, B., and Weston, S. (ed.), "State-of-the-Art Small Spacecraft Technology", NASA/TP20210021263, 131 – 135 (2021).